The Astrophysical Journal, 873:119 (11pp), 2019 March 10 https://doi.org/10.3847/1538-4357/ab074a

Timing Properties of Shocked Accretion Flows around Neutron Stars in the Presence of Cooling

Ayan Bhattacharjee[1] and Sandip K. Chakrabarti[1,2]
[1] S. N. Bose National Centre for Basic Sciences, Salt Lake, Kolkata 700106, India; ayan12@bose.res.in, chakraba@bose.res.in
[2] Indian Center for Space Physics, 43 Chalantika, Garia St. Road, Kolkata 700084, India
Received 2018 July 26; revised 2019 February 10; accepted 2019 February 13; published 2019 March 12

Abstract

We carry out the first robust numerical simulation of accretion flows on a weakly magnetized neutron star using smoothed particle hydrodynamics (SPH). We follow the two-component advective flow (TCAF) paradigm for black holes and focus only on the advective component for the case of a neutron star. This low-viscosity sub-Keplerian flow will create a Normal Boundary Layer (NBOL) right on the star surface in addition to the CENtrifugal pressure supported BOundary Layer (CENBOL) present in a black hole accretion. These density jumps could give rise to standing or oscillating shock fronts. During a hard spectral state, the incoming flow has a negligible viscosity, causing a larger sub-Keplerian component as compared to the Keplerian disk component. We show that our simulation of flows with cooling and a negligible viscosity produces precisely two shocks and strong supersonic winds from these boundary layers. We find that the specific angular momentum of matter dictates the locations and the nature of oscillations of these shocks. For flows with low angular momentum, the radial oscillation appears to be preferred. For flows with higher angular momentum, the vertical oscillation appears to become dominant. In all cases, asymmetries with respect to the $Z = 0$ plane are seen, and instabilities set in due to the interaction of the inflow and outgoing strong winds. Our results capture both the low- and high-frequency quasi-periodic oscillations without invoking magnetic fields or any precession mechanism. Most importantly, these solutions directly corroborate observed features of wind-dominated high-mass X-ray binaries, such as Cir X-1.

Key words: accretion, accretion disks – hydrodynamics – radiation: dynamics – shock waves – stars: neutron – X-rays: binaries

1. Introduction

Modeling of the accretion process around neutron stars is largely prompted by significant observational findings ever since they were discovered. Although many of the models are of great phenomenological importance, a unified solution is still not present that describes both the spectral and temporal behavior self-consistently. For black holes (BHs), a self-consistent solution that simultaneously addresses timing and spectral properties exists in the form of two-component advective flow (TCAF; Chakrabarti 1995, 1997; see also Chakrabarti & Titarchuk 1995 for some spectra of TCAF), where both the Keplerian and sub-Keplerian (low angular momentum) matter accrete together. With a goal to study the applicability of the TCAF paradigm to neutron stars, we conduct a 2D hydrodynamic simulation of an inviscid, sub-Keplerian accreting flow around a nonmagnetic neutron star. We argue that when the accretion rate is low and the viscosity parameter α is negligible, our simulations show shocks. When the viscosity is higher, a TCAF would disaggregate out of a single sub-Keplerian component flow, as happened, for example, in black hole accretion (Chakrabarti 1990, 1996; Giri & Chakrabarti 2013).

The temporal variations of both magnetic and weakly magnetic, accreting neutron stars (NSs) are reflected in the power density spectra (PDS) of the light curves at different energies. The presence and evolution of quasi-periodic oscillations (QPOs) reveal significant details about both the hydrodynamic and radiative transfer processes. We have used the definitions from Wang (2016) for the different classes of QPOs, and the corresponding abbreviations have been used throughout this paper:

1. Low-frequency QPOs (LFQPO): Low-frequency QPOs, with quality factor $Q \geqslant 2$ and amplitudes 1%–10%, are observed in the range 5–60 Hz. The flaring, normal, and horizontal branch oscillations all lie in this domain and are respectively abbreviated as FBO, NBO, and HBO.
2. Hectohertz QPOs (hHz QPO): A peaked noise usually shows up as the hHz QPO. If the peak is coherent enough to have a quality factor $Q > 2$, it is classified as a QPO. The frequency $\nu_{\rm hHz}$ is seen in the range 100–200 Hz. It has an rms amplitude between 2% and 20%.
3. Kilohertz QPOs (kHz QPO): These are, usually, defined as the QPOs in the range 200 Hz $< \nu_{\rm kHz} <$ 1300 Hz.

We take the following approach to address the validity of our solution: we point to the observational evidence that either supported the TCAF paradigm or refuted an alternate theory in light of new results. We have touched upon the relevant models in the literature and compared them in terms of predictions of observational results, as an introduction to the studies reported here. A more detailed version of this, which is summarized here, can be found in Bhattacharjee (2018).

Elsner & Lamb (1977) carried out the first detailed study of almost radial accretion onto a magnetic neutron star and discussed important properties of the magnetosphere. The spin-up and spin-down mechanisms of the star due to this were studied by Ghosh et al. (1977). The structures of the transition region and the changing period of the pulsating stars were studied by Ghosh & Lamb (1979a, 1979b). The study of the PDS of the source GX 5-1 by van der Klis et al. (1985) revealed an intensity dependence of the centroid frequency, width, and power of the observed QPOs (20 and 40 Hz) and low-frequency noises (<15 Hz). The interaction of a clumpy

disk and a weak magnetosphere was proposed as the cause of the modulation in accretion rate and oscillations in X-ray flux for the source Sco X-1, which was reflected as QPOs in the 5–50 Hz range. A bimodal behavior in the response of QPO frequency with intensity was found for Sco X-1 by Priedhorsky et al. (1986), where they showed that the 6 Hz QPO, in a quiescent state, was anticorrelated with intensity, whereas in the active state the 10–20 Hz QPOs were correlated with intensity. An unsteady flow with low viscosity was proposed by Paczynski (1987) to be the cause of the luminosity variations of the boundary. Correlation between the spectral shape, fast variability, temperature, and burst duration with accretion rate $\dot{M}$ as well as lack thereof with persistent intensity for 4U 1636-53 led van der Klis et al. (1990) to suggest that the accretion rate $\dot{M}$, which might not be well measured by intensity, determines the source state. Strohmayer et al. (1996) used a magnetospheric beat-frequency model to explain the constant separation of 363 Hz, which was equal to the burst pulsations, between the twin kHz QPOs that varied between 650 and 1100 Hz for the low-mass X-ray binary 4U 1728-34. For Sco X-1, van der Klis et al. (1997) found that the twin kHz QPO frequency separation, rather than being constant, varied from 310 to 230 Hz, and they concluded that these peaks are not likely to be explained by any photon bubble model or beat-frequency model. They also found that both of the HBOs, near 45 and 90 Hz, increased with accretion rate. The energy-dependent study of twin kHz QPOs and band-limited noise by Méndez et al. (1997) suggested that the kHz QPOs were due to oscillations of the boundary layer very close to the surface and that the broad noise was generated from near the inner edge of a disk, and these frequencies tracked $\dot{M}$ better than the count rate. Simultaneous HBOs and kHz QPOs for GX 17+2, found by Wijnands et al. (1997), suggested that the phenomena could not be simultaneously explained by the magnetospheric beat-frequency model. The rms and FWHM of the lower kHz QPO remained constant with changes in frequency, but that of the upper kHz QPO varied. The Z-source Cyg X-2 also was discovered to exhibit simultaneous kHz QPOs and HBOs by Wijnands et al. (1998b). For the Z-source GX 340+0, Jonker et al. (1998) showed that the twin kHz QPO frequencies moved to higher values with the increase in accretion rate. The rms and FWHM of the upper kHz QPO decreased, whereas the ones corresponding to the lower QPO remained generally constant. A simultaneous HBO was also detected along with its second harmonic between 20 to 50 Hz and 38 Hz and 69 Hz. They also concluded that something other than $\dot{M}$ determined the timing properties, from the study of the FWHM of HBOs with states. Wijnands et al. (1998b) observed simultaneous kHz QPOs and HBOs for the object GX 5-1 and found similar results.

In Titarchuk et al. (1998, hereafter TLM98), a super-Keplerian transition layer (TL) was invoked to explain the kHz QPOs. Méndez et al. (1998) showed a varying separation between the centroid frequencies of twin kHz QPOs of LMXB 4U 1608-522 and ruled out any simple beat-frequency model. A simultaneous existence of burst oscillation and twin KHz QPOs for 4U 1728-34 was found by Méndez & van der Klis (1999). For the same object, the TL model was used by Titarchuk & Osherovich (1999), where they attributed radial oscillation in a viscous timescale and a radial diffusion timescale as the possible determining factors behind low-Lorentzian frequency and the break frequency, respectively. A correlation between (1) the NS kHz QPOs and HBOs and (2) BH QPOs and noises, of the same type but varying three orders of magnitude in frequency and coherence, was found by Psaltis et al. (1999), who suggested that the variations are systematic and related by similar processes in the two types of compact objects. Different modes of QPOs observed for 4U 1728-34 were explained by Titarchuk et al. (1999) by adding the effects of Coriolis forces and interaction of the magnetosphere. The study of Sco X-1 by Dieters & van der Klis (2000) revealed that the position on the Z-track or the spectral state was not the only parameter that governs the behavior of the source. A new broad component in the PDS of GX 340+0 between 9 and 14 Hz was discovered by Jonker et al. (2000). For the source Sco X-1, Yu et al. (2001) found that the ratio of lower to upper kHz QPO amplitude and the upper kHz QPO frequency were anticorrelated with the count rate that varied in the NBO timescale (6–8 Hz) and suggested that some of the NBO flux was generated from inside the inner disk radius and the radiative stress modulated the NBO frequency. A long-term study of a total of 13 Z and atoll sources by Muno et al. (2002) showed that similar three-branched color–color patterns are traced out by both, which was previously not recorded because of incomplete sampling, suggesting a similarity between the two types of sources.

The decomposition of PDS into four primary Lorentzians for both BHs and NSs by Belloni et al. (2002) revealed that the physical processes of HFQPOs might be the same for both types of compact object and possibly independent of the stellar surface. In the same year, Mauche extended the QPO correlation between BH and NS to the case of white dwarfs (WDs) over five orders of magnitude, further suggesting a common mechanism of oscillations in these systems. Based on their studies of multiple accreting NSs, Wijnands et al. (2003) suggested that the QPOs can be understood in terms of resonances at specific radii in an accretion disk. Barret et al. (2005a) ruled out the possibility of any model involving clumps, and disk/shock oscillations were suggested to be the more likely mechanism of generating QPOs in LMXB 4U 1608-52. Belloni et al. (2005) showed that a biased sampling leads to the finding of a ratio of upper and lower kHz QPO frequencies of around 3/2, which indicated that a simple resonance model of a Keplerian disk is unlikely to address the kHz QPOs. From the one-to-one correspondence between the LFQPOs in BHs and NSs, inferred that the physical mechanisms that determine these oscillations are in favor of a disk origin of oscillation and rule out models involving interaction with the magnetosphere or the surface. Méndez (2006) suggested that one possible mechanism of generation of kHz QPOs would be that the mass accretion rate sets the size of the inner radius of the disk, which determines the QPO frequency as well as the relative contribution of the high-energy part of the spectrum to the total luminosity. To explain the lower value of kHz QPOs in Cir X-1, Boutloukos et al. (2006) pointed out that a high radially accreting flow is more likely than a Keplerian disk for the source. The study of NBOs for Sco X-1 by Wang et al. (2012) also suggested a radial oscillation as the centroid frequency varied nonmonotonically with energy.

2. TCAF around a Neutron Star

In Bhattacharjee & Chakrabarti (2017a), we discussed at length how the spectral signatures of TCAF are present in observations of accretion flows around neutron stars. Here, we

include more of those features that pertain to the timing properties of such flows and discuss how there is a connection between the TCAF scenario and the observed results. A detailed version of this comparative study is reported in Bhattacharjee (2018), which we summarize here. The spectral and timing properties of accreting matter around a black hole could not be explained by a standard Keplerian disk (Sunyaev & Truemper 1979; Haardt & Maraschi 1993; Zdziarski et al. 2003; Chakrabarti 1995; CT95; Chakrabarti 1997). The two main components of the spectrum are (1) a thermal component, which resembles multicolor blackbody radiation (Shakura & Sunyaev 1973), and (2) a power-law-like component generated by inverse Comptonization of the thermal or nonthermal electrons (Sunyaev & Titarchuk 1980, 1985). Although many models deal with the production of a Compton cloud that generates the power law, many such possible scenarios required excessive fine-tuning of accreting matter and are self-consistent or not physical (for a review, see Chakrabarti 2017). TCAF, which is based on the transonic flow solution, is a unique self-consistent solution (Chakrabarti 1995, 1996, 1997) equally applicable for BHs and NSs when a proper inner boundary condition is chosen. All of the aspects of spectral and temporal properties are addressed at the same time by the TCAF paradigm. In this scenario, the low-viscosity advection component produces a CENtrifugal-pressure supported BOundary Layer (CENBOL) very close to a compact object. A shock transition defines the boundary of CENBOL. This shock surface may be stationary, oscillating, or propagatory (Chakrabarti 2017 and references therein). The postshock region behaves as a natural reservoir of hot electrons. The highly viscous component of the flow near the equatorial plane becomes a Keplerian disk (Giri & Chakrabarti 2013). This disk emits a multicolor blackbody radiation that is intercepted and reradiated by the CENBOL to create the power-law-like component (Chakrabarti 1997; Garain et al. 2014, hereafter GGC14). The power-law component usually has an exponential cutoff where recoil becomes important.

The shock formed in the transonic flows around BHs and NSs can oscillate due to resonance (Molteni et al. 1996a, hereafter MSC96) or nonsatisfaction of the Rankine–Hugoniot condition (Ryu et al. 1997). The variation in the size of the CENBOL results in modulation of intensity of the hard X-ray, manifesting as the LFQPOs. The CENBOL also acts as the source of outflows and jets. When excessive soft photons cool the CENBOL down, the jet disappears as well. There is clear observational evidence of TCAFs in several black hole candidates (Smith et al. 2001, 2002; Debnath et al. 2013; Mondal et al. 2014; Dutta & Chakrabarti 2016; Bhattacharjee et al. 2017; Ghosh & Chakrabarti 2018).

A natural explanation of the phenomenological Compton clouds for the black hole accretion can be found in the TCAF paradigm. Apart from the region near the innermost boundary, the flow accreting from the outer edge of the disk has little knowledge about the nature of the compact object. Therefore, we anticipate, especially when the magnetic field is weak ($<10^8$ Gauss), even an NS accretion would have a CENBOL that forms away from the surface of the NS. The advective matter almost freely falls under gravity until it reaches the surface of the NS. Thus, in a neutron star accretion, two shocked layers would be simultaneously present: one is similar to the normal boundary layer (NBOL), and the other is similar to the CENBOL in a black hole accretion (Chakrabarti 1995). Only CENBOL is present in a black hole accretion. In the following discussion, we point to some of the key similarities between the TCAF scenario and the flow configuration demanded by observations. The conclusions of Chakrabarti (1996) and Chakrabarti & Sahu (1997), that the boundary condition of the gravitating object (BH or NS) modifies the solutions of the transonic flows only in the last few Schwarzschild radii, are strengthened by these points.

The following observed features can be reproduced when the accretion flow on a neutron star is TCAF:

1. The low-frequency QPOs ($\nu_{\rm LF}$) show a bimodal behavior (Priedhorsky et al. 1986): The intensity is controlled by two separate accretion rates. One increases the oscillation radius, and another reduces it.
2. BHs, NSs, and WDs show correlated QPOs (Psaltis et al. 1999; Belloni et al. 2002; Mauche 2002): A stellar surface or magnetosphere should not be required by the generalized model.
3. Sources of varying intensity have similar kHz QPO frequency ($\nu_{\rm kHz}$; Méndez et al. 1998): More than one accretion rate controls the QPOs.
4. The kHz QPOs have a long coherence time (Barret et al. 2005b): Vertical and radial oscillations would be preferred. It is unlikely that clumpy disk models with azimuthal asymmetry would generate QPOs in a Keplerian orbital timescale.
5. A "mass" accretion rate that controls the relative contribution to the high-energy part of the spectrum also decides the inner edge of the disk that generates kHz QPOs (Méndez 2006).
6. The Compton cloud acts as the base of the jet (Paizis et al. 2006).
7. The state transition was controlled by more than just a single accretion rate (Barret 2001; Barret & Olive 2002).
8. Some NSs (For Cir X-1, Boutloukos et al. 2006) show low $\nu_{\rm kHz}$: An advective flow (radial accretion) is preferred over a Keplerian disk.

We divide our study of accretion flow into two broad classes: (1) The flow is inviscid, advective, and has a low efficiency of radiation. It also comprises winds from the companion star. (2) The flow has a significant viscosity to create TCAF and has a disk emitting blackbody radiation.

The main focus of the present work is to concentrate on Class 1 flows, namely, the effect of angular momentum of a sub-Keplerian flow in the absence of significant dynamic viscosity. In such a scenario, which can occur when the accretion rate is relatively low as compared to the Eddington limit, we assume the bremsstrahlung cooling to be the dominant process. These classes are not that well explored in the literature as in the case of black hole accretion using hydrodynamic simulations, and thus we focus on this domain of solutions first. However, when the viscosity is high enough to produce a Keplerian disk on the equatorial plane, the blackbody emission from the disk as well as the nonlocal cooling processes such as Comptonization would become significant. Those aspects of Class 2 flows are not within the scope of this paper and will be discussed in a subsequent paper (A. Bhattacharjee and S. K. Chakrabarti 2019, in preparation). TLM98 and subsequent works have tried to explore this domain, although with the assumption that the entire disk is Keplerian to begin with. In Bhattacharjee & Chakrabarti (2017,

hereafter BC17), we have shown similarities and differences between the TLM98 scenario and the TCAF paradigm in spectral analysis and will carry out a timing study in a subsequent paper.

3. Method

The smoothed particle hydrodynamics (SPH) method was introduced by Monaghan (1992). It has since been used in many astrophysical systems, including simulation of accreting matter around black holes to simulate accretion in 1D (Chakrabarti & Molteni 1993, hereafter CM93), 2D flows (Molteni et al. 1994, hereafter MLC94), viscous Keplerian disks (Chakrabarti & Molteni 1995, hereafter CM95), resonance oscillation of shocks due to cooling in 2D (MSC96), a comparative study of shocked advective flows using SPH and total variation diminishing (TVD) schemes (Molteni et al. 1996a, hereafter MRC96), thick accretion disks (Lanzafame et al. 1998, hereafter LMC98), bending instability of an accretion disk (Molteni et al. 2001a, hereafter M01a; Molteni et al. 2001b, hereafter M01b), interaction of accretion shocks with winds (Acharya et al. 2002, hereafter ACM02), and the effect of cooling on the time-dependent behavior of accretion flows (Chakrabarti et al. 2004, hereafter CAM04).

We base our studies of accretion onto a neutron star mostly on MSC96, though we modify the SPH algorithm to suit our need to handle both hot and cold particles in the neutron star environment.

3.1. Model Equations

We consider a rotating, axisymmetric, inviscid flow around a neutron star. We consider the magnetic field to be negligible and ignore its effects completely. The gravitational force due to the compact object was modeled using the pseudo-Newtonian potential of Paczyński & Wiita (1980). The matter density (ρ), isotropic pressure (P), and internal energy (e) of the flow are related to each other through $P = \rho e(\gamma - 1)$. The adiabatic index $\gamma = 4/3$ is kept constant throughout our simulations. We used a single-temperature model for the electrons and protons. The specific angular momentum λ is varied from case to case but is constant everywhere in a simulation setup, as the flow is purely inviscid. Furthermore, the SPH code uses toroidal particles, and thus it strictly preserves λ. The hydrodynamic code uses dimensionless quantities for computation. However, the cooling mechanisms require physical units (cgs units are used here). For that purpose, all of the relevant quantities are nondimensionalized using their corresponding reference values. We use the density of injected particles of the flow at the outer edge $\rho_{\rm ref} = \rho_0$, the speed of light $v_{\rm ref} = c$, and the Schwarzschild radius $x_{\rm ref} = r_S = 2GM_{\rm NS}/c^2$ of the neutron star mass $M_{\rm NS}$ as the reference density, velocity, and distance, respectively. From that we can derive the units of time $t_{\rm ref} = x_{\rm ref}/v_{\rm ref} = r_S/c$, specific angular momentum $\lambda_{\rm ref} = x_{\rm ref}v_{\rm ref} = cr_S$, mass $M_{\rm ref} = \rho_{\rm ref}x_{\rm ref}^3 = \rho_{\rm ref}r_S^3$, and mass accretion rate $\dot{M}_{\rm ref} = \rho_{\rm ref}x_{\rm ref}^3/t_{\rm ref} = \rho_{\rm ref}r_S^3 c$.

We provide the Lagrangian formulae for the two-dimensional fluid dynamics equations for SPH in cylindrical coordinates below.

The conservation of mass is given as (LMC98)

$$\frac{D\rho}{Dt} = -\rho\,\boldsymbol{\nabla}\cdot\boldsymbol{v} \tag{1}$$

(here, D/Dt is the comoving derivative).

The conservation of momentum is given by (LMC98, dropping the viscous terms from Equation (2))

$$\frac{D\boldsymbol{v}}{Dt} = -\frac{1}{\rho}\boldsymbol{\nabla}P + \boldsymbol{g} + \frac{\lambda^2}{r^3}\hat{r}, \tag{2}$$

where $\hat{r}$ is the radial direction vector and

$$\boldsymbol{g} = -\frac{1-\mathcal{C}}{2(R-1)^2}\frac{\boldsymbol{R}}{R}, \tag{3}$$

$$g_r = -\frac{1-\mathcal{C}}{2(R-1)^2}\frac{r}{R}, \tag{4}$$

$$g_z = -\frac{1-\mathcal{C}}{2(R-1)^2}\frac{z}{R}. \tag{5}$$

Here, $\boldsymbol{R} = r\hat{r} + z\hat{z}$, $R = \sqrt{r^2+z^2}$, and $\mathcal{C}$ is the radiative pressure term arising out of the blackbody emission from the surface of the star. We have assumed the term to be isotropic for our simulations.

To achieve a better accuracy, we use a form of energy conservation where the sum of kinetic and thermal energies is used instead of only thermal energy (Monaghan 1985). Then, the energy conservation can be written as (following Equation 9(c) of MSC96 and Equation (11) of LMC98)

$$\frac{D}{Dt}\left(e + \frac{1}{2}\boldsymbol{v}^2\right) = -\frac{P}{\rho}\boldsymbol{\nabla}\cdot\boldsymbol{v} + \boldsymbol{v}\cdot\left(\frac{D\boldsymbol{v}}{Dt}\right) - \zeta_{1/2}\rho e^{\alpha}. \tag{6}$$

Here, $\zeta_{1/2}$ is the nondimensional bremsstrahlung loss coefficient, as defined in MSC96,

$$\zeta_{1/2} = \frac{j\rho_{\rm ref}x_{\rm ref}T_{\rm ref}^{1/2}}{c^3 m_p^2} \tag{7}$$

and

$$T_{\rm ref} = \frac{c^2 m_p \mu(\gamma-1)}{k}, \tag{8}$$

where $\mu = 0.5$ and $j = 1.4\times10^{-27}$ cgs unit for ionized hydrogen (Allen 1973), m_p is the mass of the proton, and k is the Boltzmann constant. The subscript $1/2$ to ζ signifies the use of a cooling law $\Lambda = \zeta_{1/2}\rho^2 e^{\alpha}$ with a constant $\zeta_{1/2}$, which is identical to the bremsstrahlung case ($\alpha = 0.5$).

3.2. SPH: Implementation of the Cooling Law

We use the method described in detail by MSC96 while making changes to match the notations used so far. We have assumed the flow to be axisymmetric, so all of the equations are written for a cylindrical geometry. The interpolating kernel is W, which is a function of cylindrical radial coordinate $\boldsymbol{R}$ and the kth particle of mass m_k as (MSC96)

$$m_k = 2\pi\rho_k r_k \Delta\boldsymbol{R}_k. \tag{9}$$

Any smooth function $A(\boldsymbol{R}_i)$ at position $\boldsymbol{R}_i$ can be defined as (MSC96)

$$A(\boldsymbol{R}_i) = \int A(\boldsymbol{R})W(\boldsymbol{R}-\boldsymbol{R}_i;h)\frac{2\pi\rho r}{2\pi\rho r}d\boldsymbol{R}_k \approx \sum_k \frac{m_k}{2\pi\rho_k r_k}A(\boldsymbol{R}_k)W(\boldsymbol{R}_k-\boldsymbol{R}_i;h), \tag{10}$$

where h is the particle size. This simplifies the expression of the conservation laws and quantities that can be computed easily. As an example, the density at position $\boldsymbol{R}_i$ can be simplified as

$$\rho(\boldsymbol{R}_i) \approx \sum_k \frac{m_k}{r_k} W(\boldsymbol{R}_k - \boldsymbol{R}_i; h), \tag{11}$$

which satisfies the continuity equation in cylindrical coordinates (MSC96).

The equations of motion to be solved using SPH are reduced to three separate ones: the radial component of the momentum equation,

$$\left(\frac{Dv_r}{Dt}\right)_i = \sum_k \frac{m_k}{r_k}\left(\frac{P_i}{\rho_i^2} + \frac{P_k}{\rho_k^2} + \Pi_{ik}\right)\frac{\partial W_{ik}}{\partial r_i} + \frac{\lambda^2}{r_i^3} - \frac{1-\mathcal{C}}{2(R_i-1)^2}\frac{r_i}{R_i}, \tag{12}$$

the vertical component of the momentum equation,

$$\left(\frac{Dv_z}{Dt}\right)_i = \sum_k \frac{m_k}{r_k}\left(\frac{P_i}{\rho_i^2} + \frac{P_k}{\rho_k^2} + \Pi_{ik}\right)\frac{\partial W_{ik}}{\partial z_i} - \frac{1-\mathcal{C}}{2(R_i-1)^2}\frac{z_i}{R_i}, \tag{13}$$

and the specific energy equation, which can be written as

$$\left(\frac{D(e+\boldsymbol{v}^2/2)}{Dt}\right)_i = \sum_k \frac{m_k}{r_k}\left(\frac{P_i}{\rho_i^2} + \frac{P_k}{\rho_k^2} + \Pi_{ik}\right) - \frac{\Lambda_i}{\rho_i} + \boldsymbol{v}_i \cdot \left(\frac{D\boldsymbol{v}}{Dt}\right)_i, \tag{14}$$

where $\Lambda_i = \zeta_{1/2}\rho_i^2(e_i)^\alpha$ is the cooling term.

The kinematic dissipation is mimicked using artificial viscosities (MSC96):

$$\Pi_{ij} = \frac{\alpha_v \mu_{ij}\bar{c}_{ij} + \beta\mu_{ij}^2}{\bar{\rho}_{ij}},$$
$$\mu_{ij} = \frac{r_i v_{ri} - r_j v_{rj}}{r_i(l_{ij}^2 + \eta_{ij}^2)} + \frac{(v_{zi}-v_{zj})(z_i - z_j)}{(l_{ij}^2+\eta_{ij}^2)},$$
$$l_{ij}^2 = (r_i - r_j)^2 + (z_i - z_j)^2,\ \eta_{ij} = \eta = 0.1h^2,$$

where α_v and β are the artificial viscosity coefficients.

Equations (12)–(14) have been adopted from MSC96 and LMC98, with the introduction of the term $\mathcal{C}$. Note that the kinematic viscosity modifies the energy significantly but does not modify the angular momentum beyond 0.05% of the initial value. Thus, our simulations effectively reproduce the flow with constant angular momentum. The abbreviations for density $\bar{\rho}_{ij}$ and sound speed $\bar{a}_{ij}$ are taken from Monaghan (1992):

$$\bar{\rho}_{ij} = \frac{\rho_i + \rho_j}{2},\ \bar{a}_{ij} = \frac{a_i + a_j}{2}.$$

3.3. Conservation of Angular Momentum

We have used the following equation (LMC98 and MSC96) for the conservation of angular momentum:

$$\left(\frac{Dv_\phi}{Dt}\right)_i = -\left(\frac{v_\phi v_r}{r}\right)_i + \frac{1}{\rho_i}\left[\frac{1}{r^2}\frac{\partial}{\partial r}\left(r^3\mu_{ij}\frac{\partial}{\partial r}\left(\frac{v_\phi}{r}\right)\right)\right]_i, \tag{15}$$

where μ_{ij} is the kinematic viscosity. The terms α_v and β control the amount of μ_{ij} necessary to reduce oscillations in shock transitions. However, the second term is much less than the first term on the right-hand side and makes no significant contribution. We determined the value of $\lambda_i = r_i(v_\phi)_i$ for the particle and use it in Equation (12). It was observed that, for all of the cases we have tried, the determined angular momentum was almost constant and equal to the injected values up to an error of 0.05%. The average value over all particles deviated even less from the injected value, for example, for C1, $\lambda_{\rm avg} = 1.800001$, matching the injected value up to five decimal places. This little numerical error is due to the fluctuation of the values of $(v_\phi)_i$ and $(v_r)_i$. Thus the obtained values of λ_i are effectively equal to the λ of the injected particles, which is obtained as a natural consequence of the conservation of angular momentum throughout the flow. As the flow is always sub-Keplerian, it can continue to the inner boundary, which is the surface of the star. A part of the flow is absorbed into the star beyond $R = R_{\rm NS}$, where the rotational velocity matches that of the star and the surplus rotational kinetic energy is released through $\Delta\mathcal{E}(t)$ (see the section on boundary conditions). As an example, the rate of transport of angular momentum onto the star for C1, that is, the spin-up torque $N \approx \dot{M}_{\rm accr}\lambda$, was such that the spin-up rate $\dot{\nu} = N/2\pi I$ was roughly around $5 \times 10^{-14}\,{\rm Hz\,s^{-1}}$, where the moment of inertia $I \approx 0.4 M_{\rm NS}R_{\rm NS}^2$. Thus any change of the spin of the star due to this feedback effect can be safely ignored for the purpose of calculations for the run times we have chosen.

3.4. Boundary Conditions

For our simulations, the pseudoparticles (or just "particles" in the text) are injected from $r_{\rm inj} = 30\,r_S$ with the same specific energy and specific angular momentum. The flow is assumed to be in vertical equilibrium when injected. The particles are tracked as long as they are within $r < r_{\rm inj}$ and $R < R_{\rm out}$, where $R_{\rm out} = 35\,r_S$. The choice of $R_{\rm out}$ was made so as to minimize the computational time taken to track isolated particles moving far away from the inflow region. We have also carried out our simulations for a rectangular simulation box, but no significant changes were observed. For C1, the injection velocity was done at the equatorial plane with $v = 0.1202$ and sound speed $a = 0.0586$, which are appropriate values for the transonic branch. Similarly, for cases C2 to C5, to ensure injection with the same total energy and Mach number, we had to choose $v = 0.1211$ and $a = 0.0590$. In order to implement a reflection boundary condition at the inner boundary of $R_i < R_{\rm NS} + h$, we used a reflecting condition for the velocity component v_R. For the v_θ component, a sliding or slipping boundary condition is used, where the flow maintains its v_θ value at the surface. The choice of boundary condition for the v_ϕ component was based on both physical and numerical factors. We have tried multiple scenarios involving the presence and absence of absorption conditions and the effect of no-slip and slip conditions with zero and nonzero viscosity. What we found was that inviscid, sub-Keplerian flows reaching the surface of the star would undergo the following processes: piling up at the boundary $\longrightarrow$ forming a highly dense layer $\longrightarrow$ a local increase in viscosity $\longrightarrow$ redistribution of the angular momentum to match the v_ϕ of the layer with that of the star $\longrightarrow$ being absorbed, effectively.

Table 1
Parameters for the Simulations and Centroid Frequencies (in Hz) Found in the PDS of Bremsstrahlung Loss

ID	$\dot{m}_h$ ($\dot{M}_{\rm EDD}$)	$\lambda(r_S c)$	$R_{\rm NS}$ (r_S)	α	$\nu_{\rm LF1}$, $Q_{\rm LF1}$	$\nu_{\rm LF2}$, $Q_{\rm LF2}$	$\nu_{\rm hHz}$, $Q_{\rm hHz}$	ν_l, Q_l	ν_u, Q_u
C1	0.094	1.8	3.0	0.5	⋯	⋯	128.88, 17.82	213.31, 3.17	⋯
C2	0.094	1.7	3.0	0.5	⋯	⋯	102.22, 3.91	425.40, 5.61	633.78, 1.77
C3	0.188	1.7	3.0	0.5	⋯	⋯	115.55, 5.02	486.08, 2.49	742.73, 1.48
C4	0.094	1.7	3.0	0.6	41.62, 1.30	94.41, 4.66	137.58, 5.78	434.97, 4.96	599.23, 3.51
C5	0.094	1.7	4.0	0.5	36.36, 2.91	77.55, 3.14	196.11, 18.06	465.70, 5.11	654.67, 3.51

Numerically, the most efficient scheme for inviscid flows turned out to be the one with "no-slip" and absorption, after reaching the surface, which implicitly takes care of the mentioned steps. The explicit study of viscous flows, with different inner boundary conditions and the transition mentioned above, is beyond the scope of the present work and will be reported in a separate paper, as stated earlier. Thus, for the cases reported here, a no-slip condition is used for the azimuthal component where the v_ϕ of the flow is matched with the angular velocity of the star ($\omega_{\rm NS} r_{\rm NS}$) at the surface. For our calculations, $\omega_{\rm NS} = 142$ Hz. Along with the cooling criteria, these conditions allow matter to settle down on the surface of the star and also allows meridional motion from the equatorial region toward the poles (and vice versa). However, if the flow reaches $R_i = R_{\rm NS}$, it is immediately absorbed, and all of the thermal and kinetic energy of the particle is assumed to be released as blackbody radiation. In the present simulations, we did not study the emission due to Comptonization of seed photons originating from bremsstrahlung or blackbody radiation. We did, however, include the effects of radiation pressure on the flow through the quantity $\mathcal{C}$. We report the cases where the temperature is self-consistently modified by taking into account the additional flux arising from the energy of the accreted particles. The initial surface temperature $T^0_{\rm NS}$ of the neutron star was kept constant for all cases (C1 to C5) at $T^0_{\rm NS} = 0.0$ keV. The term $\mathcal{C}$ is controlled by the total energy deposited by the particles at the surface of the star ($\Delta\mathcal{E}$), and it is given by

$$\mathcal{C}(t) = \frac{T^4_{\rm NS}(t)\sigma_{bb} R^2_{\rm NS} m_p}{c\sigma_T}, \text{ where } T_{\rm NS}(t) = \left((T^0_{\rm NS})^4 + \frac{\Delta\mathcal{E}(t)}{\sigma_{bb} 4\pi R^2_{\rm NS} dt}\right)^{0.25}. \quad (16)$$

Here, σ_{bb} is the Stefan–Boltzmann constant, m_p is the mass of proton, and σ_T is the Thompson scattering cross section.

3.5. Coalescence of Particles

One of the major problems with the previous version of the code was that it did not dynamically evolve when the particles came very close to each other ($R_{ij} < h$), and the resulting hydrodynamical timescale became very small. This problem is even more acute in our case as particles tend to aggregate on the surface of the star. In the original code, within 150 time steps the value of dt reached <0.0002 and effectively stopped the evolution. A simple absorption condition at the boundary did not solve the problem as the aggregates grew beyond the surface's immediate vicinity. To circumvent this, we implemented a two-particle coalescing scheme (adopted from Vacondio et al. 2013) when the interparticle distance $R_{ij} < 0.1\,h$.

After each time step, we check for neighbors using a linked-list algorithm. The neighbor list of a particle i is then searched for all such neighbors j for which $R_{ij} < 0.1\,h$. The minimum of such R_{ij} values and the corresponding (i, j) pair is selected. If such pairs are found, a list of such pairs is made, and the following scheme is applied to coalesce particle pairs (i, j).

To conserve the total mass,

$$m_k = m_i + m_j,\ k = \min(i, j). \quad (17)$$

We preserve the total momentum using

$$\boldsymbol{v}_k = \frac{m_i \boldsymbol{v}_i + m_j \boldsymbol{v}_j}{m_i + m_j}. \quad (18)$$

We also preserve the total thermal energy using

$$e_k = \frac{m_i e_i + m_j e_j}{m_i + m_j}. \quad (19)$$

The new location of the particle is determined by

$$\boldsymbol{R}_k = \frac{m_i \boldsymbol{R}_i + m_j \boldsymbol{R}_j}{m_i + m_j}. \quad (20)$$

After going through the list of all such pairs, a standard re-indexing is done for all of the particles still left in the system. As a result, the average number of particles present in the simulation stayed between ∼14,000 and ∼16,000 for C1 and between ∼11,500 and ∼13,000 for C2–C5.

3.6. Timing Analysis

We computed the total emitted energy due to bremsstrahlung $\mathcal{E}(t)$ by integrating the emission per unit mass (Λ_i/ρ_i) over the particles existing in the simulation (n):

$$\mathcal{E}(t) = \sum_{i=1}^{i=n} \Lambda_i m_i/\rho_i. \quad (21)$$

As a consequence, the densest and hottest regions contributed more to the time variation of the bremsstrahlung loss. In order to probe the hydrodynamic characteristics of CENBOL and NBOL, the emitted energy was plotted against time to generate the light curve. To extract periodic features, we used NASA's FTOOLS package to create the fast Fourier transformed PDS from the light curves. Data were gathered after every 10^{-5} s to generate the light curve. We used the POWSPEC command with a rebinning factor of -1.05 for all of the cases to generate the PDS. Any oscillatory signature (such as a quasi-periodic oscillation or a peaked noise) is reflected as a peak in the PDS. We report only those five cases (see Table 1) where significant variations of QPOs are observed. To avoid the effects of the transient phase, we only used data collected from 0.05 s to 0.3286 s. A Lorentzian profile is used to fit a QPO in the PDS. We determined the centroid frequencies, FWHM, and rms power up to the 90% confidence level. While fitting the

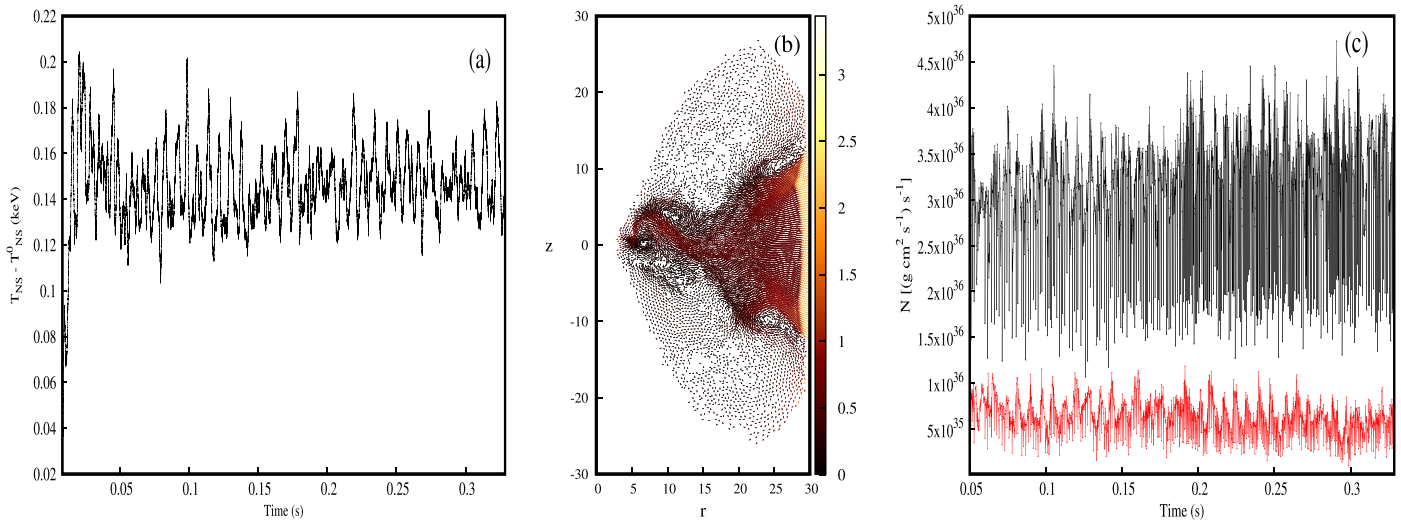

Figure 1. (a) Variation of $T_{\rm NS}$ with time (s); (b) the velocity vector $v_r\hat{r} + v_z\hat{z}$ (arrowheads) with the Mach number in the color bar for the flow configuration C1 at time $t = 0.2690$ s; (c) variation of the rate of transfer of angular momenta (N) onto the surface of the star (black) and in the outflows (red) with time (s).

QPOs with Lorentzians, we only fitted the fundamental frequency of a type of QPO, when the harmonic overlaps with another fundamental frequency. In the case of such an overlap, we take the best statistical fit (one peak or a mean position as the case demanded). When no such overlap occurs and the harmonic feature is significant, the corresponding Lorentzian is fitted and mentioned in the text (Table 1).

4. Results

We studied multiple cases (see Table 1) by varying the specific angular momentum (λ), radius of the star ($R_{\rm NS}$), accretion rate ($\dot{m}$, alternatively used as the halo accretion rate $\dot{m}_h$), and cooling index (α), one at a time, to study the effects in accretion and outflow.

We first discuss a typical scenario in detail to highlight the hydrodynamical aspects of the flow.

Case C1: In order to demonstrate hydrodynamic properties, we first focus on case C1. The initial simulation parameters are mentioned in Table 1. The simulation was run for 32,860 time steps ($t = 0.3286$ s), which is equivalent to 200 dynamical time steps at $30\,r_S$. The cooling process was switched on after $t \sim 0.0083$ s. The system settled into a steadily oscillating state after a brief transient phase (up to $t \sim 0.0500$ s). Indeed, the temperature of NBOL was found to fluctuate around 0.15 keV even though initially its value was chosen to be ∼0.0 keV. Figure 1(a) shows the variation of the NBOL temperature during our simulation. This would induce fluctuations of the NBOL height as well. Details of the behavior of NBOL are beyond the scope of the current paper and will be published elsewhere. In this case, we studied the PDS of the mass outflown through the upper quadrant. The hectohertz frequency corresponding to vertical oscillation was found at $\nu_{\rm hHz} = 127.22$ Hz, with a harmonic at $\nu_{\rm hHz} = 254.40$ Hz. For black holes, Molteni et al. (2001a) found such oscillations were due to bending instabilities in the flow. When scaled for the mass of the neutron star (here assumed to be $M_{\rm NS} = 1.0\,M_\odot$ for computational purposes), the frequency range comes out as 20–300 Hz. Thus, we can clearly identify the oscillations in the light curve as well as the mass outflow that are due to such instabilities, which are also reflected in Figures 2(c)–(d).

In Figure 1(b), the velocity in the $r - z$ plane is plotted for all of the particles. The Mach number values are shown in the color gradient. Multiple turbulent cells are seen to be formed by the interaction of wind and accreting matter. The formation of an outflow, in both the upper and lower quadrants, from the postshock region of CENBOL is also captured. In the lower quadrant, a portion of the outflow falls back onto the inflow as a feedback.

In Figure 1(c), the variation of the rate of transfer of angular momentum (N, see Section 3.3) with time is plotted for accretion (black) and outflows (red). Given that the specific angular momentum of the flow remains constant, the variation of the transfer rate with time depends on the mass flow rate in accretion and outflow, respectively. As the flow is always sub-Keplerian, the solution allows the matter to fall onto the star and transfer the angular momentum on the surface of the star. However, the spin-up torque (N) plotted in the figure was such that it corresponded to a spin-up rate of $\sim 5.0 \times 10^{-14}$ Hz s^{-1}. The value agrees well with observational results and predictions from other models (Bildsten 1998; Revnivtsev & Mereghetti 2015; Bhattacharyya & Chakrabarty 2017b; Gügercinoğlu & Alpar 2017; Sanna et al. 2017; Ertan 2018). The rest of the angular momentum is carried out by the outflows in both quadrants.

In Figure 2(a), we show the density contours [$\log(\rho/\rho_0)$]. The temperature contours (logarithmic scale) are plotted in Figure 2(b). The contours of constant Mach number for accreting matter, at time $t = 0.2690$ s, are shown in Figure 2(c). Panel 2(d) shows the Mach number contours for the same case C1, at time $t = 0.2528$ s. The flow puffs up after the centrifugal pressure supported shock (CENBOL) and acts as the base of the outflowing matter. The matter nearest the star is observed to be the hottest and densest. A dense and hot outflow is seen to emerge from within the CENBOL region. The Mach number contours show that the flow has a time-dependent asymmetric distribution about the $z = 0$ plane. For C1, the high angular momentum creates the outer shock at around 26 r_S on the equatorial plane. The subsonic flow beyond the shock surface slowly becomes supersonic near the inner boundary of the star and finally settles on the surface through a strong shock. Notice that the Mach number contours near the

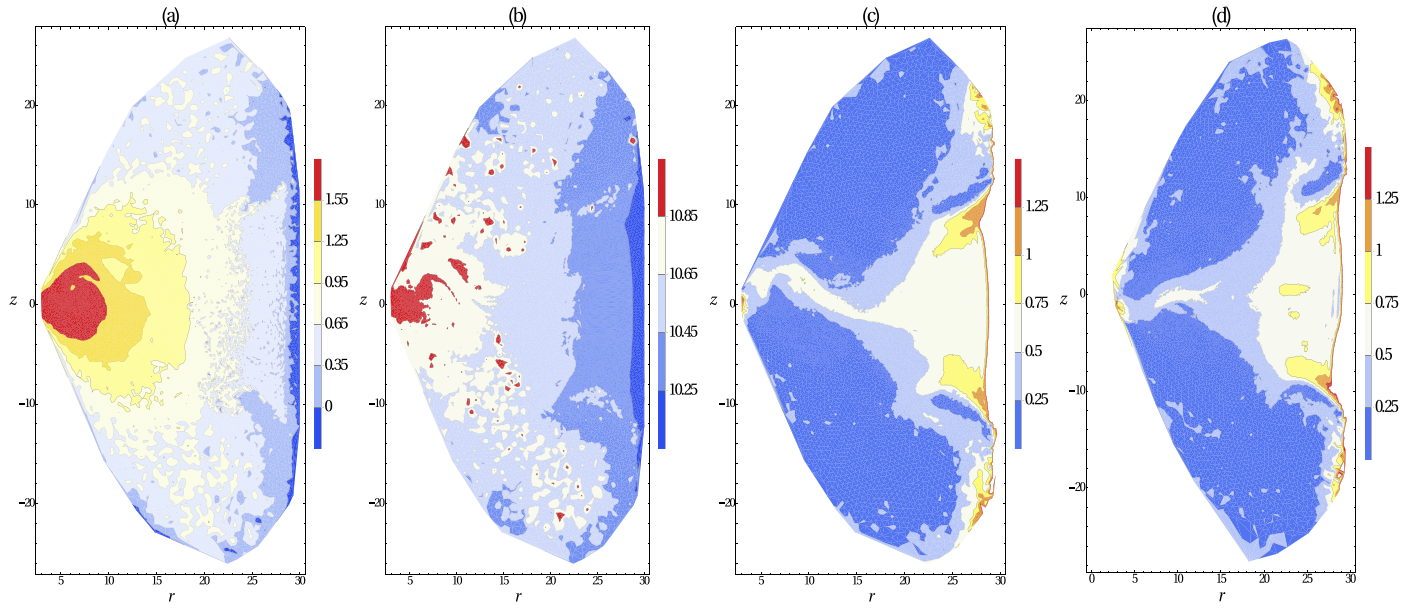

Figure 2. Flow configuration for case C1: (a) $\log(\rho/\rho_0)$, (b) log of temperature in K, (c) Mach number contours for accreting inviscid flow at $t = 0.269$ s and at (d) $t = 0.2528$ s. Both the density and temperature change by an order of magnitude in the inner part of CENBOL, as compared to the outer part. The flow configuration in (c) shows only the preshock region of the secondary shock (NBOL) at the boundary. However, in (d), we see that the shock has formed at $\sim 5\ r_S$, and a shock in outflow forms very close to the surface of the star. The outflow (in both (c) and (d)) becomes supersonic near the outer edge of the simulation boundary.

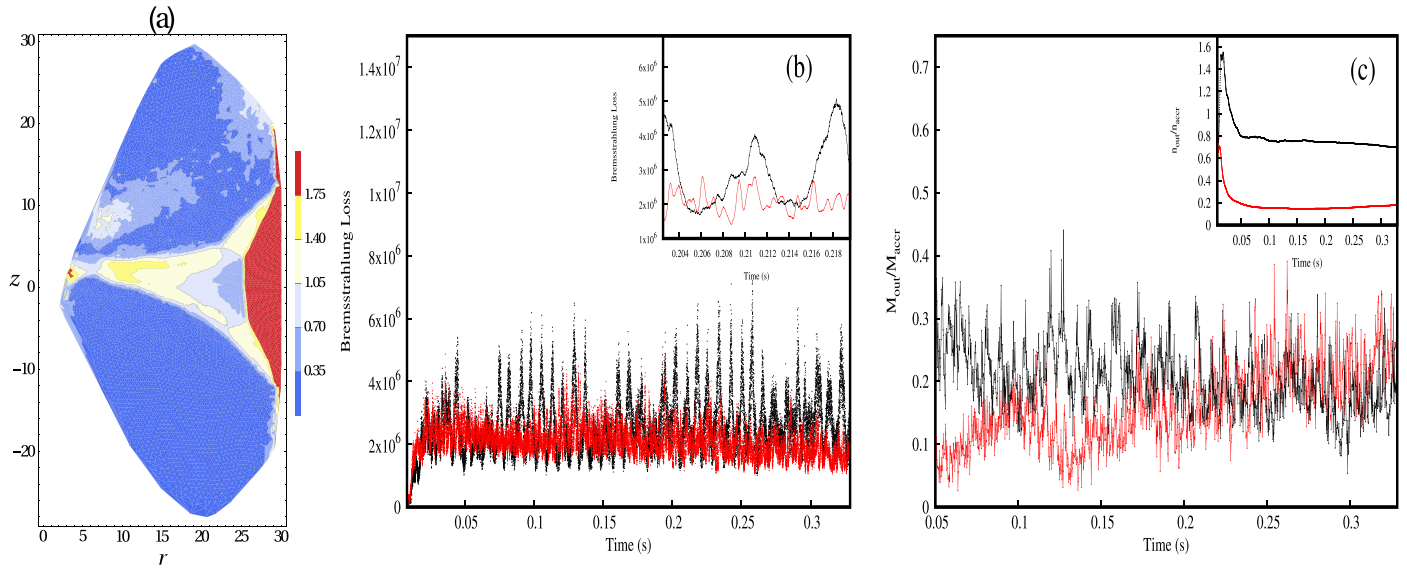

Figure 3. (a) Contours of constant Mach number for case C2 at time $t = 0.269$ s. The outer shock forms closer to the star at $\sim 25\ r_S$. The inner shock is formed at $\sim 5\ r_S$. The shock in outflow is diffused as compared to C1 and is formed between ~ 10 and $15\ r_S$. The outflow became transonic near the outer edge. In (b), we show the light curves of the total bremsstrahlung loss from the system for cases C1 (black) and C2 (red). Both light curves show a periodic behavior with distinctly different frequencies. In (c), the ratio $M_{\rm out}/M_{\rm accr}$ ($=\dot{M}_{\rm out}/\dot{M}_{\rm accr}$) for both C1 (black) and C2 (red) is plotted. The inset of (c) shows the $n_{\rm out}/n_{\rm accr}$ ratio ($=\dot{n}_{\rm out}/\dot{n}_{\rm accr}$), which shows more particles were coalesced near the NS boundary, and the outflow generated from the regions closer to the NS surface had a low $n_{\rm out}/n_{\rm accr}$ value despite having comparable $M_{\rm out}/M_{\rm accr}$ values.

edge of the star show the supersonic behavior of the flow, and no contours of subsonic Mach number are plotted. This is because, in the plotted case, the shock surface was very close to the boundary and the subsonic pseudoparticles were absorbed at the surface, before being written out, within the code.

Case C2: When λ is reduced from 1.8 to 1.7, it reduces the asymmetry around the $z = 0$ plane (Figure 3(a)). The shock near the star becomes more prominent, and the outflow profile changes. For C1, most of the outflow is generated from the immediate vicinity of the postshock region of the CENBOL. We plot the ratio of the mass outflow to the mass accreted onto the star in unit time (denoted by $\dot{M}_{\rm out}/\dot{M}_{\rm accr} = M_{\rm out}/M_{\rm accr}$) for both C1 and C2 in Figure 3(c). Apart from the initial higher values for C1, the ratio is comparable. However, the particle-coalescing scheme merges the particles in a higher density region, which reduces the number of particles in the simulation. The inset panel of Figure 3(c) shows the same comparison in terms of the ratio of number of particles outflown to the number of accreted particles in unit time (denoted by $\dot{n}_{\rm out}/\dot{n}_{\rm accr} = n_{\rm out}/n_{\rm accr}$). The lower value for C2 further affirms the fact that the bulk of the outflow is generated near the NBOL for C2. The outflow in Figure 3(a) also undergoes a shock

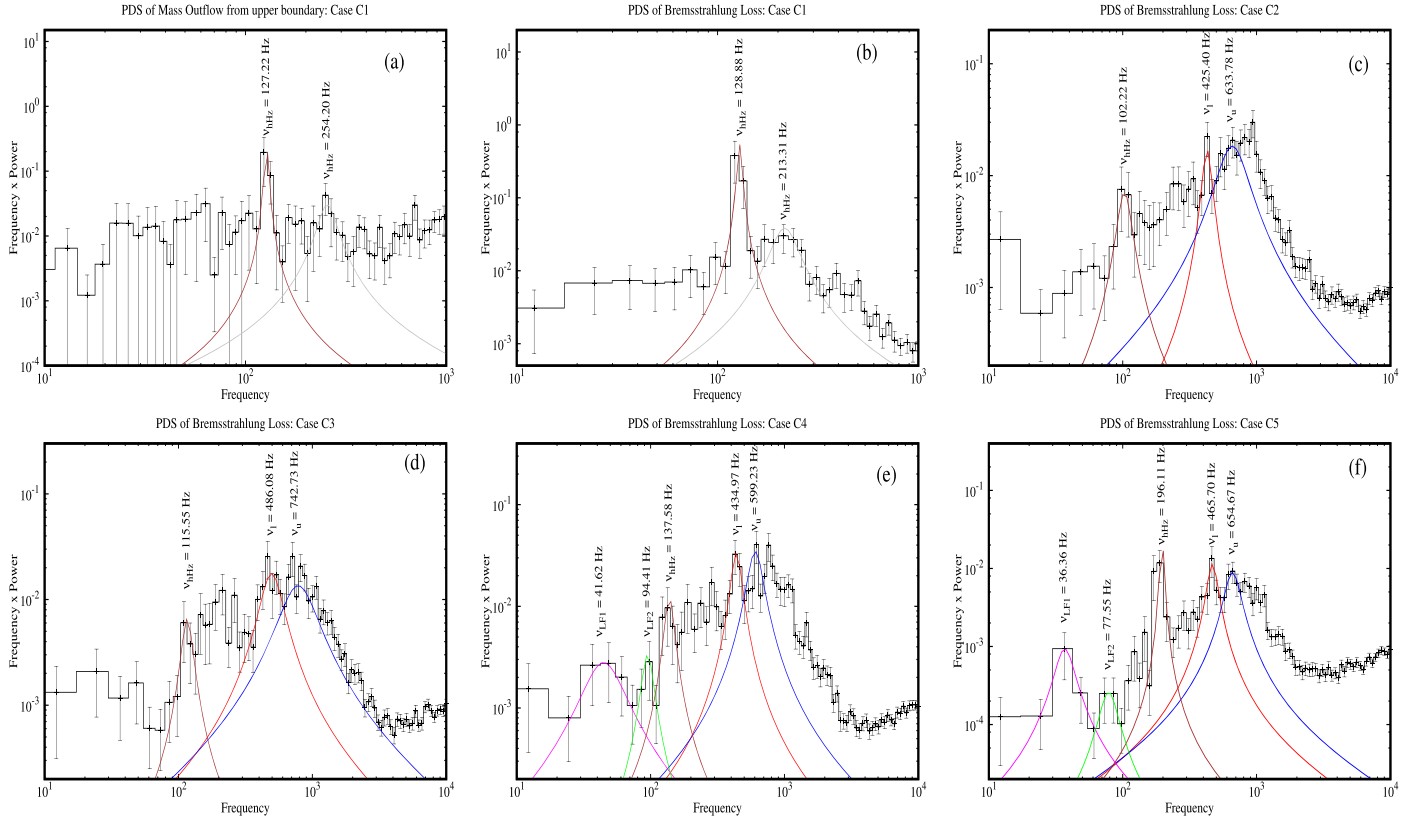

Figure 4. (a) Power density spectrum (frequency × power vs. frequency) of the mass outflow from the upper quadrant of the simulation setup for case C1. A clear QPO at ∼127 Hz with a harmonic at ∼254 Hz is observed. (b) A similar QPO feature at ∼129 Hz was found in the corresponding light curve of the bremsstrahlung loss. The PDS of bremsstrahlung loss for (c) C2, (d) C3, and (e) C4 is also shown. The clear harmonics of the kHz QPOs and the influence of those in the power spectra have been ignored while fitting separate peaks (b)–(e). In (f), for case C5, only the second harmonic of $\nu_{\rm LF}$ is shown. For that, five distinct peaks have been fitted with Lorentzian profiles, having centroid frequencies at 36.36 Hz (magenta, $\nu_{\rm LF1}$), 77.55 Hz (green, $\nu_{\rm LF2}$), 196.11 Hz (brown, $\nu_{\rm hHz}$), 465.70 Hz (red, ν_l), and 654.67 Hz (blue, ν_u), which are also plotted.

transition before becoming transonic again. In Figure 4(c), we plot the PDS of bremsstrahlung loss for the case C3. As λ was decreased from 1.8 to 1.7, the centrifugal-pressure-dominated force is decreased. However, the flow was injected with the same total energy as in case C1, which resulted in a higher radial velocity. This increases the ram pressure of the fluid flow and prompts the resonance oscillation to take place at a smaller radius. The resulting oscillations are also seen to be dominated by the radial motion as compared to the vertical motion. The CENBOL moves closer to the star surface. The hectohertz QPO is still present and observed at $\nu_{\rm hHz} = 102.22$ Hz. We also observe the twin kHz QPOs between 400 and 700 Hz. The centroid frequencies of the lower and upper kHz QPOs are at $\nu_l = 425.40$ Hz and $\nu_u = 633.78$ Hz, respectively.

Case C3: In Figure 4(d), we plot the PDS of bremsstrahlung loss for C3. As $\dot{m}_h$ was increased from 0.094 to 0.188, the effective radiative cooling due to the bremsstrahlung process is also increased (higher ρ). The decrease in cooling timescale prompts the resonance oscillation to take place at a smaller radius. This brings the NBOL closer to the surface. The hectohertz QPO is also observed at $\nu_{\rm hHz} = 115.55$ Hz. Both the lower and upper kHz QPOs show an increase in centroid frequency (compared to C2) at $\nu_l = 486.08$ Hz and $\nu_u = 742.73$ Hz, respectively.

Case C4: As α was increased from 0.5 to 0.6, the effective radiative cooling due to the bremsstrahlung process decreased (lower Λ). The increase in cooling timescale prompts the resonance oscillation to take place at a larger radius. This pushes the NBOL away from the surface. The PDS of bremsstrahlung loss for case C4 is shown in Figure 4(e). The low-frequency QPOs are observed at $\nu_{\rm LF1} = 41.62$ Hz and at $\nu_{\rm LF2} = 94.41$ Hz. The hectohertz QPO is also observed at $\nu_{\rm hHz} = 137.58$ Hz. Both the lower and upper kHz QPOs are also observed at $\nu_l = 434.97$ Hz and $\nu_u = 599.23$ Hz, respectively.

Case C5: In this case, as $R_{\rm NS}$ was increased from 3 r_S to 4 r_S, the effective radiative pressure due to the blackbody emission from the surface of the star decreased (lower $\mathcal{C}$). This aided the gravitational force in bringing both of the shocks closer to the surface. The reduction of the outer edge of CENBOL increased the centroid frequency, above 10 Hz, corresponding to the low-frequency QPO $\nu_{\rm LF1} = 36.36$ Hz and its harmonic $\nu_{\rm LF2} = 77.55$ Hz, making them detectable (Figure 4(f)). The hectohertz QPO is also observed at $\nu_{\rm hHz} = 196.11$ Hz. Both the lower and upper kHz QPOs are also observed at $\nu_l = 465.70$ Hz and $\nu_u = 654.67$ Hz, respectively.

5. Conclusions

In this paper, we have made an effort to understand the dynamics of an inviscid, rotating, geometrically thick and optically thin flow around a weakly magnetic neutron star using SPH. We add modified bremsstrahlung cooling so as to particularly study the timing properties of the centrifugally driven shocks (CENBOL) as well as the density jump (NBOL) formed on the star surface due to the sudden arrest of infalling

matter. Such simulations were done *for black holes* earlier (MLC94, MSC96, MRC96, M01a, M01b, ACM02, CAM04, GC13, GGC14, Deb et al. 2017), and oscillations of the CENBOL were found in the radial and vertical directions. These oscillations were then identified with the low-frequency QPOs observed in black hole candidates.

In the presence of a hard boundary on the neutron star surface, we expect another oscillation of higher frequency as well as others due to nonlinear interactions of the flows. Our present simulations indeed show complex timing properties of the radiation as well as the flow dynamics. For this, we chose the flow to have an accretion rate ($\dot{m}_h$) below the Eddington limit for all of the cases we studied. The exponent α in the cooling rate was varied from 0.5 (bremsstrahlung) to 0.6 to observe the effects of the strength of cooling on the oscillation of shocks. The specific angular momentum λ was chosen based on the recent study by Deb et al. (2017), where an onset of vertical oscillation was seen between the two values chosen here. The variation of the radius of the neutron star had a more complex effect as it controlled the effects of radiation pressure on the hydrodynamics through the parameter $\mathcal{C}$ when a self-consistent variation is chosen. Note also that for the timescales of simulations C1 to C5, the mass and momentum deposited on the star were negligible as compared to the star's mass and spin. This accumulation of mass and momentum would become significant for timescales of the order of years or more, which is outside the purview of the current paper. However, the energy release at the surface was found to be significant, resulting in a measurable change of $T_{\rm NS}$.

We show, among other things, that the simulations produce both low- and high-frequency QPOs, and the oscillations last during the whole simulation period (more than 200 dynamical timescales measured at the injected flow radius, i.e., $30\,r_S$). This suggests that the QPOs are formed from a part of the flow dynamics and are not a transient effect, as inferred by others (e.g., Barret et al. 2005b). We measure the QPO frequencies and find that both the centroid frequencies and Q factors match well with the observed results of neutron stars such as GX17 +2, 4U 1728-34, and Cir X-1. We believe that the advective flow suggested in the literature, while explaining the behavior of the source Cir X-1 (Boutloukos et al. 2006), may be the same as the dynamic transonic flow solution we discuss here. We showed that the presence of angular momentum itself can generate multiple modes of oscillation in CENBOL and NBOL, manifesting as QPOs in the PDS, in the presence of cooling. In Figures 1(b), 2(c)–(d), and 3(a), we see different types of shocks are being formed. The outer shock was found to be vertical near the equatorial plane and oblique away from the plane, very similar to what was seen for simulations around black holes (MLC94). The bending instabilities reported in M01a are also found here and correspond to the hectohertz oscillations found in the PDS.

So far, in the literature, a model that appears to be capable of phenomenologically addressing both timing and spectral properties is the TL model of TLM98, who assumed the disk to be Keplerian to begin with. The viscosity was also assumed to be high enough to maintain a Keplerian distribution. The QPOs are then explained as the oscillation of the TL at different orbital frequencies. An extended TL was used in the COMPTT and COMPTB models for the analysis of spectra of accreting NSs. Many low-mass X-ray binaries have been studied using the COMPTB framework, such as 4U 1728-34 (Seifina & Titarchuk 2011), GX 3+1 (Seifina & Titarchuk 2012), GX 339+0 (Seifina et al. 2013), 4U 1820-30 (Titarchuk et al. 2013), Scorpius X-1 (Titarchuk et al. 2014), and 4U 1705-44 (Seifina et al. 2015). The high-mass X-ray binary 4U 1700-37 has also been examined using the same model (Seifina et al. 2016). Two COMPTB components were needed in general for spectral fitting. The one corresponding to a cloud closer to the star had a relatively lower temperature, and the one closer to the Keplerian disk typically had a higher temperature (see the works cited above). The one corresponding to Comptonization of NS surface photons showed a saturation in the spectral index of the COMPTB model (Farinelli & Titarchuk 2011). This index is different from the spectral index found by fitting the power-law component of the spectrum. The latter can have a continuous range of values depending on the two accretion rates, as shown in BC17. However, since the source of high viscosity required to sustain a complete Keplerian distribution remains elusive, and physical processes to create two Compton clouds out of a Keplerian disk are also not demonstrated, we preferred to start with a sub-Keplerian inviscid advective flow onto a neutron star, which is a general configuration. In the presence of higher turbulent viscosities, this flow will become a Keplerian disk easily, as in the case of black hole accretion, by simply redistributing angular momentum (Chakrabarti 1990, 1996, 2017), and thus in softer states the flow could resemble a configuration similar to the TLM98 model. In general, the flow should have both the sub-Keplerian and Keplerian components (Chakrabarti 1995, 1997, 2017, CT95). The infall timescales from Chakrabarti (1995; see also Chakrabarti 1997) have the similar $r^{3/2}$ dependence with the radial distance r. The absolute value only differs from the Keplerian orbital timescale by a factor of $R_{\rm comp}/2\pi$, $R_{\rm comp}$ being the shock compression ratio. This, in principle, suggests that the same numerical values of frequencies for all such sources could be produced by the TCAF scenario, even when the flow is non-Keplerian to begin with and the viscosity is too low to form any TL. The preshock and postshock regions of NBOL are orders of magnitude denser than those of CENBOL and contribute to higher frequency oscillations as well. In the TCAF scenario, the physical NS boundary aids in the formation of the inner shock (NBOL) apart from the CENBOL surface, which is formed even in BH accretion.

We found that the ratio ν_u/ν_l varied from 1.38 to 1.53 and the ratio $\nu_l/\nu_{\rm hHz}$ varied from 1.66 to 4.20 in our simulations. The Q factors of lower kHz QPOs were always found to be greater than the Q factor of the upper one. This agrees well with observational results (Barret et al. 2005a). In our cases, the separation $\delta\nu$ between ν_u and ν_l increased with accretion rate, which is similar to the results from Cir X-1 (Boutloukos et al. 2006). In fact, the values of Table 1, when scaled with the mass of Cir X-1, lie in the same ballpark as those found in observation.

In passing, we mention that our simulation clearly demonstrated that the advective flows onto a nonmagnetic neutron star create a stable configuration. The flow with a sub-Keplerian specific angular momentum has at least two density jumps in accretion, and shocks were also found in the outflows. In the presence of cooling, the shocks underwent oscillations in both the radial and vertical directions and were manifested as QPOs in the PDS of bremsstrahlung loss from the system. We also find that the shock locations, and hence the QPO frequencies,

depend on many parameters of the flow, specifically, the specific angular momentum λ, the accretion rate $\dot{m}_h$, the radius of the star $R_{\rm NS}$, and the strength of cooling α, which we studied here.

The most general flow configuration should depend on the spin, mass, and radius of the star and the viscosity of the flow. In this paper, we kept the spin frequency constant at 142 Hz, the mass was kept constant at 1.0, and viscous effects were ignored. In a future paper, we will vary these crucial parameters and generate a spectrum of steady and oscillating solutions. Nonlocal cooling processes and an electron energy distribution due to shock acceleration are yet to be incorporated in the simulation. From the results of BC17, it is clear that when accretion rates are high for a hot accretion flow, Compton cooling has a significant effect on the temperature of the flow. In the future, we wish to couple a Monte Carlo simulation with this hydrodynamic code to get a time-dependent spectral variation. The results would be presented elsewhere.

A.B. would like to acknowledge Prof. D. Molteni and Dr. G. Lanzafame for their 2D SPH simulation source code, written by them with S.K.C., which was modified for the case of a neutron star with cooling and particle-coalescing schemes to produce the results used in this paper.

ORCID iDs

Ayan Bhattacharjee https://orcid.org/0000-0002-2878-4025
Sandip K. Chakrabarti https://orcid.org/0000-0002-0193-1136

References

Acharya, K., Chakrabarti, S. K., & Molteni, D. 2002, JApA, 23, 155
Allen, C. W. 1973, Astrophysical Quantities (London: Athlone)
Barret, D. 2001, AdSpR, 28, 307
Barret, D., Kluźniak, W., Olive, J. F., Paltani, S., & Skinner, G. K. 2005a, MNRAS, 357, 1288
Barret, D., & Olive, J.-F. 2002, ApJ, 576, 391
Barret, D., Olive, J.-F., & Miller, M. C. 2005b, MNRAS, 361, 855
Belloni, T., Méndez, M., & Homan, J. 2005, A&A, 437, 209
Belloni, T., Psaltis, D., & van der Klis, M. 2002, ApJ, 572, 392
Bhattacharjee, A. 2018, in Exploring the Universe: From Near Space to Extra-galactic, Astrophysics and Space Science Proceedings, Vol. 53, ed. B. Mukhopadhyay & S. Sasmal (Heidelberg: Springer), 93
Bhattacharjee, A., Banerjee, I., Banerjee, A., Debnath, D., & Chakrabarti, S. K. 2017, MNRAS, 466, 1372
Bhattacharjee, A., & Chakrabarti, S. K. 2017a, MNRAS, 472, 1361
Bhattacharyya, S., & Chakrabarty, D. 2017b, ApJ, 835, 4
Bildsten, L. 1998, in AIP Conf. Ser. 431, Accretion processes in astrophysical systems: Some like it hot!, ed. S. S. Holt & T. Kallman (Melville, NY: AIP), 299
Boutloukos, S., van der Klis, M., Altamirano, D., et al. 2006, ApJ, 653, 1435
Casella, P., Belloni, T., & Stella, L. 2005, ApJ, 629, 403
Chakrabarti, S. K. 1995, in Ann. N. Y. Acad. Sci. 759, Seventeenth Texas Symp. Relativistic Astrophysics and Cosmology, ed. H. Bohringer, G. E. Morfil, & J. Truemper (New York: New York Academy of Sciences), 546
Chakrabarti, S., & Titarchuk, L. G. 1995, ApJ, 455, 623
Chakrabarti, S. K. 1990, MNRAS, 243, 610
Chakrabarti, S. K. 1996, ApJ, 464, 664
Chakrabarti, S. K. 1997, ApJ, 484, 313
Chakrabarti, S. K. 2017, in Proc. 14th Marcel Grossman Meeting on General Relativity, ed. M. Bianchi, R. Ruffini, & R. Jantzen (Singapore: World Scientific), 369
Chakrabarti, S. K., Acharyya, K., & Molteni, D. 2004, A&A, 421, 1
Chakrabarti, S. K., & Molteni, D. 1993, ApJ, 417, 671 (CM93)
Chakrabarti, S. K., & Molteni, D. 1995, MNRAS, 272, 80
Chakrabarti, S. K., & Sahu, S. A. 1997, A&A, 323, 382
Deb, A., Giri, K., & Chakrabarti, S. K. 2017, MNRAS, 472, 1259
Debnath, D., Chakrabarti, S. K., & Nandi, A. 2013, AdSpR, 52, 2143
Dieters, S. W., & van der Klis, M. 2000, MNRAS, 311, 201
Dutta, B. G., & Chakrabarti, S. K. 2016, ApJ, 828, 101
Elsner, R. F., & Lamb, F. K. 1977, ApJ, 215, 897
Ertan, Ü. 2018, MNRAS, 479, L12
Farinelli, R., & Titarchuk, L. 2011, A&A, 525, A102
Garain, S. K., Ghosh, H., & Chakrabarti, S. K. 2014, MNRAS, 437, 1329
Ghosh, A., & Chakrabarti, S. K. 2018, MNRAS, 479, 1210
Ghosh, P., & Lamb, F. K. 1979a, ApJ, 232, 259
Ghosh, P., & Lamb, F. K. 1979b, ApJ, 234, 296
Ghosh, P., Lamb, F. K., & Pethick, C. J. 1977, ApJ, 217, 578
Giri, K., & Chakrabarti, S. K. 2013, MNRAS, 430, 2836
Gügercinoğlu, E., & Alpar, M. A. 2017, MNRAS, 471, 4827
Haardt, F., & Maraschi, L. 1993, ApJ, 413, 507
Jonker, P. G., van der Klis, M., Wijnands, R., et al. 2000, ApJ, 537, 374
Jonker, P. G., Wijnands, R., van der Klis, M., et al. 1998, ApJL, 499, L191
Lanzafame, G., Molteni, D., & Chakrabarti, S. K. 1998, MNRAS, 299, 799
Mauche, C. W. 2002, ApJ, 580, 423
Méndez, M. 2006, MNRAS, 371, 1925
Méndez, M., & van der Klis, M. 1999, ApJL, 517, L51
Méndez, M., van der Klis, M., van Paradijs, J., et al. 1997, ApJL, 485, L37
Méndez, M., van der Klis, M., Wijnands, R., et al. 1998, ApJL, 505, L23
Molteni, D., Acharya, K., Kuznetsov, O., Bisikalo, D., & Chakrabarti, S. K. 2001a, ApJL, 563, L57
Molteni, D., Fauci, F., Gerardi, G., et al. 2001b, JKAS, 34, 247
Molteni, D., Lanzafame, G., & Chakrabarti, S. K. 1994, ApJ, 425, 161
Molteni, D., Ryu, D., & Chakrabarti, S. K. 1996a, ApJ, 470, 460
Molteni, D., Sponholz, H., & Chakrabarti, S. K. 1996b, ApJ, 457, 805
Monaghan, J. J. 1985, CoPhR, 3, 71
Monaghan, J. J. 1992, ARAA, 30, 543
Mondal, S., Debnath, D., & Chakrabarti, S. K. 2014, ApJ, 786, 4
Muno, M. P., Remillard, R. A., & Chakrabarty, D. 2002, ApJL, 568, L35
Paczynski, B. 1987, Natur, 327, 303
Paczyński, B., & Wiita, P. J. 1980, A&A, 88, 23
Paizis, A., Farinelli, R., Titarchuk, L., et al. 2006, A&A, 459, 187
Priedhorsky, W., Hasinger, G., Lewin, W. H. G., et al. 1986, ApJL, 306, L91
Psaltis, D., Belloni, T., & van der Klis, M. 1999, ApJ, 520, 262
Revnivtsev, M., & Mereghetti, S. 2015, SSRv, 191, 293
Ryu, D., Chakrabarti, S. K., & Molteni, D. 1997, ApJ, 474, 378
Sanna, A., Riggio, A., Burderi, L., et al. 2017, MNRAS, 469, 2
Seifina, E., & Titarchuk, L. 2011, ApJ, 738, 128
Seifina, E., & Titarchuk, L. 2012, ApJ, 747, 99
Seifina, E., Titarchuk, L., & Frontera, F. 2013, ApJ, 766, 63
Seifina, E., Titarchuk, L., & Shaposhnikov, N. 2016, ApJ, 821, 23
Seifina, E., Titarchuk, L., Shrader, C., & Shaposhnikov, N. 2015, ApJ, 808, 142
Shakura, N. I., & Sunyaev, R. A. 1973, A&A, 24, 337
Smith, D. M., Heindl, W. A., Markwardt, C. B., & Swank, J. H. 2001, ApJL, 554, L41
Smith, D. M., Heindl, W. A., & Swank, J. H. 2002, ApJ, 569, 362
Strohmayer, T. E., Zhang, W., Swank, J. H., et al. 1996, ApJL, 469, L9
Sunyaev, R. A., & Titarchuk, L. G. 1980, A&A, 86, 121
Sunyaev, R. A., & Titarchuk, L. G. 1985, A&A, 143, 374
Sunyaev, R. A., & Truemper, J. 1979, Natur, 279, 506
Titarchuk, L., Lapidus, I., & Muslimov, A. 1998, ApJ, 499, 315
Titarchuk, L., & Osherovich, V. 1999, ApJL, 518, L95
Titarchuk, L., Osherovich, V., & Kuznetsov, S. 1999, ApJL, 525, L129
Titarchuk, L., Seifina, E., & Frontera, F. 2013, ApJ, 767, 160
Titarchuk, L., Seifina, E., & Shrader, C. 2014, ApJ, 789, 98
Vacondio, R., Rogers, B. D., Stansby, P. K., Mignosa, P., & Feldman, J. 2013, CMAME, 256, 132
van der Klis, M., Hasinger, G., Damen, E., et al. 1990, ApJL, 360, L19
van der Klis, M., Jansen, F., van Paradijs, J., et al. 1985, Natur, 316, 225
van der Klis, M., Wijnands, R. A. D., Horne, K., & Chen, W. 1997, ApJL, 481, L97
Wang, J. 2016, IJAA, 6, 82
Wang, J., Chang, H.-K., & Liu, C.-Y. 2012, A&A, 547, A74
Wijnands, R., Homan, J., van der Klis, M., et al. 1997, ApJL, 490, L157
Wijnands, R., Homan, J., van der Klis, M., et al. 1998a, ApJL, 493, L87
Wijnands, R., Méndez, M., van der Klis, M., et al. 1998b, ApJL, 504, L35
Wijnands, R., van der Klis, M., Homan, J., et al. 2003, Natur, 424, 44
Yu, W., van der Klis, M., & Jonker, P. G. 2001, ApJL, 559, L29
Zdziarski, A. A., Lubiński, P., Gilfanov, M., & Revnivtsev, M. 2003, MNRAS, 342, 355